A Prognostic Turbulence Scheme for the Nonhydrostatic Plume Model ATHAM

MICHAEL HERZOG

Department of Atmospheric, Oceanic, and Space Sciences, University of Michigan, Ann Arbor, Michigan

JOSEF M. OBERHUBER

German Climate Computing Center, Hamburg, Germany

HANS-F. GRAF

Max-Planck Institute for Meteorology, Hamburg, Germany

(Manuscript received 9 September 2002, in final form 28 May 2003)

ABSTRACT

The presented turbulence scheme was developed for the Active Tracer High-Resolution Atmospheric Model (ATHAM) to parameterize the effect of subgrid-scale turbulence. In contrast to the commonly used assumption of local isotropy in high-resolution atmospheric modeling, this scheme differentiates between horizontal and vertical turbulent exchange to represent the strong influence of buoyancy forces and vertical transports. Its computational efficiency is similar to classical turbulent kinetic energy approaches while preserving one of the main feature of higher-order schemes. The present extensions to include anisotropic effects in a turbulent kinetic energy approach do not need any ad hoc assumptions and are equivalent to the classical formulation in the isotropic limit.

The presence of high tracer concentrations in a particle-laden plume is taken into account, as well as supersonic effects at low Mach numbers. The turbulent exchange coefficients used in the equations of motion are derived from a set of three coupled differential equations for the horizontal and vertical turbulent energy and the turbulent length scale. No turbulent equilibrium is assumed. All turbulent quantities are treated prognostically.

Numerical simulations of convective plumes of a typical Plinian volcanic eruption with the nonhydrostatic plume model ATHAM reveal that a complex treatment of turbulent quantities is necessary in order to capture the bulk characteristics of the plume, such as the plume height, the horizontal extent, and plume development in time. Anisotropic effects of turbulence have a significant impact on the stability and internal structure of the plume. For the first time, results from a fully three-dimensional simulation of a volcanic plume are presented.

Because of its general formulation the presented turbulence scheme is suitable for a wide range of atmospheric applications.

1. Introduction

In today's high-resolution atmospheric models, subgrid-scale turbulence is commonly parameterized based on a prediction of the total turbulent kinetic energy. For recent reviews and intercomparisons of large-eddy simulations (LES) and cloud resolving models, see Agee and Gluhovsky (1999), Moeng et al. (1996), and Bretherton et al. (1999) and references therein. Although more sophisticated and more general turbulence parameterizations exist for a long time (e.g., Lewellen 1977), they are not widely used in practical problems for several reasons. In fully second-order closure models, the computational effort is more then doubled since transport equations need to be solved for each individual component of the Reynold stress tensor. In convective turbulence additional equations for the turbulent flux and variance of the potential temperature need to be parameterized. In order to obtain these equations closure models for the higher-order turbulence correlations must be provided, which have uncertain physical foundation (Speziale 1987). However, second-order closure schemes have the advantage of incorporating history-dependent nonlocal effects.

By identifying the vertical axis with one of the principal axis in convective atmospheric problems and focusing on the autocorrelations in the Reynold stress tensor we avoid the assumption of local isotropy in schemes based on the total turbulent kinetic energy. At the same time we keep the computational efficiency of a total turbulent kinetic energy scheme. In our new scheme the vertical turbulent exchange coefficients differ from those for horizontal turbulent exchange.

Corresponding author address: Dr. Michael Herzog, Department of Atmospheric, Oceanic, and Space Sciences, University of Michigan, 2455 Hayward Street, Ann Arbor, MI 48109.
E-mail: herzogm@umich.edu

High-reaching volcanic plumes are driven by strong buoyancy forces. However, positive buoyancy can only be produced by a dilution of the erupting hot gas particle mixture whose initial density exceeds that of the surrounding atmosphere at the vent. The amount of entrainment is a key factor that determines if the plume partially or totally collapses. Therefore, the description of turbulent processes is crucial in order to simulate the dynamic of a volcanic plume. Due to limits in the grid resolution only the large-scale turbulent eddies are explicitly resolved. Subgrid scale turbulent motions must be treated using a suitable turbulent scheme.

After a brief description of the Active Tracer High-Resolution Atmospheric Model (ATHAM), we will present our turbulence scheme and discuss results from simulations and sensitivity tests applying this new turbulence scheme.

2. The model concept

ATHAM is designed to simulate explosive volcanic eruptions for a given forcing as a lower boundary condition. Since the aim of our investigations is to link the volcanic eruption to the large-scale atmospheric flow and chemistry, phenomena inside the volcano's vent on the scale of a meter can be ignored. Based on the assumption of small particles, the behavior of the gas particle mixture can be described by five prognostic equations for the three momentum components, the pressure, and the temperature. For each tracer, one additional transport equation has to be solved.

In the present version, ATHAM consists of five modules. The dynamic part solves the Navier–Stokes equation for a gas particle mixture including the transport of active tracers (Oberhuber et al. 1998). Active tracers can occur in any concentration and can have a strong impact on the dynamics of the system. The turbulence closure scheme, which will be described in the following sections, computes turbulent exchange coefficients for each dynamic quantity. The microphysics is based on a Kessler-type parameterization and describes condensation and formation of precipitation. The connected changes in internal energy can have a strong impact on the plume dynamics. All phases of water are included: vapor, liquid, and solid (Herzog et al. 1998). Two additional modules that are not used for this study treat the interaction of gases, hydrometeors, and ash particles in the plume (Textor 1999; Textor et al. 2003): the ash module describes particle growth and coagulation based on microphysical interactions between hydrometeors and ash particles; the scavenging module calculates the dissolution of volcanic gases into droplets and the incorporation of these gases into ice particles.

The model is written in a modular structure. It is easy to add additional modules of different levels of sophistication for special processes.

ATHAM is three-dimensionally formulated with an implicit time stepping scheme. Since the flow close to vent can be supersonic, sound waves cannot be excluded from the dynamic equations. The solution of the complete Navier–Stokes equation is computed on a Cartesian grid. A grid stretching allows us to use a higher spatial resolution in the model center than at the model boundaries. The flux form of the transport equations is employed for all tracers.

For sensitivity studies, ATHAM can be used in a two-dimensional mode. The Cartesian 2D version performs simulations on a vertical slice of the 3D model. In addition, cylindrical coordinates can be used: no cross-wind effects can be studied, but the dillution of the plume corresponds to the 3D case in an atmosphere at rest.

3. The turbulence scheme

The general idea underlying our model is similar to that of a large-eddy model in which the large-scale motions are explicitly represented while the subscale turbulence is parameterized. If ϕ denotes a quantity to be calculated, we set

$$\phi(x, y, z, t) = \overline{\phi}(x, y, z, t) + \phi'(x, y, z, t), \quad (1)$$

where x and y are horizontal Cartesian coordinates, z the vertical coordinate, t time, the overbar denotes a spatial average over a volume given by a model grid box, and the prime denotes the fluctuations from the average. ATHAM explicitly calculates the spatial averages, which represent the dominant large-scale motions while parameterizing the effects of the fluctuations (which we call the ''turbulence'') on the averaged flow quantities. Here $\overline{\phi}$ is assumed to be a traditional Reynolds average (i.e., $\overline{\overline{\phi}} = \overline{\phi}$ and $\overline{\phi'} = 0$) so that Leonard stresses and subgrid-scale cross stresses can be neglected [for the definition of Leonard stresses and subgrid-scale cross stresses see Speziale (1998)].

Applying expression (1) introduces turbulent correlations $\overline{\phi' u_i'}$ in the dynamic equations, where u_i denotes a velocity component $(u_1, u_2, u_3) = (u, v, w)$. We identify the turbulent correlations with the subscale fluxes, which describe the effect of turbulence on the averaged flow quantities. Under the assumption that turbulence acts like diffusion, subgrid fluxes can be parameterized by a gradient approach (Monin and Yaglom 1971):

$$\overline{\phi' u_i'} = -K_{ik} \frac{\partial}{\partial x_k} \overline{\phi}. \quad (2)$$

In kinetic energy methods, the tensor K_{ik} is assumed to be diagonal and isotropic (Harsha 1977):

$$K_{ik} = K\delta_{ik}. \quad (3)$$

The turbulent exchange coefficient K is set proportional to a turbulent length scale λ and the square root of the turbulent energy $E = \overline{u'u'} + \overline{v'v'} + \overline{w'w'}$ (Kolmogorov 1942; Prandtl and Wieghardt 1945):

$$K = c_0 \lambda \sqrt{E}. \quad (4)$$

An empirical constant is c_0. However, in general, the

two-dimensional tensor K_{ik} is only diagonal if the chosen coordinate axes are identical to the principal axes. The choice of the principal axes must be independent from the specific location in space, since the dynamic equations should be valid for each location in space. In atmospheric problems, the vertical can be identified with one principal axis. The mean horizontal wind direction defines another principal axis. However, since the mean wind direction varies in space and time, no distinction between the horizontal axes is possible. There is experimental evidence (Monin and Yaglom 1971) that it is sufficient to treat K_{ik} as diagonal matrix

$$K_{ik} = K_{ik}\delta_{ik} = K_k. \tag{5}$$

Therefore, we assume K_{ik} to be diagonal, but we distinguish between the horizontal and vertical exchange coefficient:

$$K_1 = K_2 = K_{\text{hor}} = c_0\lambda\sqrt{3/2E_{\text{hor}}}, \tag{6}$$

$$K_3 = K_{\text{ver}} = c_0\lambda\sqrt{3E_{\text{ver}}}, \quad \text{with} \tag{7}$$

$$E_{\text{hor}} = \overline{u_1'u_1'} + \overline{u_2'u_2'}, \tag{8}$$

$$E_{\text{ver}} = \overline{u_3'u_3'}. \tag{9}$$

The horizontal and vertical component of the turbulent kinetic energy are denoted by E_{hor} and E_{ver}, respectively. In the limit case of a local isotropy $\overline{u_1'u_1'} = \overline{u_2'u_2'} = \overline{u_3'u_3'} = 1/3E$, (6) and (7) are equivalent to the classical formulation in (4).

In order to derive prognostic equations for E_{hor} and E_{ver} we use the Navier–Stokes equation for an incompressible medium and ignore the Coriolis force:

$$\frac{\partial}{\partial t}\rho u_i = -\frac{\partial}{\partial x_k}\rho u_i u_k - \frac{\partial}{\partial x_i}P - \rho g\delta_{i3} + \frac{\partial}{\partial x_k}\mu\frac{\partial}{\partial x_k}u_i,$$

$$\frac{\partial}{\partial x_k}\rho u_k = 0. \tag{10}$$

Splitting pressure, density and velocity components into mean and turbulent part in Eq. (10), and assuming $\rho' \ll \overline{\rho}$, we yield after subtracting the turbulence averaged equation

$$\frac{\partial}{\partial t}\overline{\rho}u_i' = -\frac{\partial}{\partial x_k}\overline{\rho}(u_i'u_k' + u_i'\overline{u_k} + \overline{u_i}u_k' - \overline{u_i'u_k'}) - \frac{\partial}{\partial x_i}P' - \rho' g\delta_{i3} + \frac{\partial}{\partial x_k}\mu\frac{\partial}{\partial x_k}u_i'. \tag{11}$$

Multiplying Eq. (11) by u_j and adding the j component of (11) multiplied by u_i, we yield after turbulence averaging an equation for the turbulent velocity correlations:

$$\begin{aligned}
&\frac{\partial}{\partial t}\overline{\rho}\overline{u_i'u_j'} \\
&= -\frac{\partial}{\partial x_k}\overline{\rho}\,\overline{u_k}\overline{u_i'u_j'} && \text{advection} \\
&\quad - \frac{\partial}{\partial x_k}\overline{\rho}\overline{u_k'u_i'u_j'} && \text{turbulent diffusion} \\
&\quad + \frac{\partial}{\partial x_k}\mu\frac{\partial}{\partial x_k}\overline{u_i'u_j'} && \text{molecular diffusion} \\
&\quad - \overline{\rho}\left(\overline{u_j'u_k'}\frac{\partial}{\partial x_k}\overline{u_i} + \overline{u_i'u_k'}\frac{\partial}{\partial x_k}\overline{u_j}\right) && \text{production by wind shear} \\
&\quad - g(\overline{u_i'\rho'}\delta_{j3} + \overline{u_j'\rho'}\delta_{i3}) && \text{production by buoyancy} \\
&\quad - \overline{u_j'\frac{\partial}{\partial x_i}P'} - \overline{u_i'\frac{\partial}{\partial x_j}P'} && \text{redistribution} \\
&\quad - 2\mu\overline{\left(\frac{\partial}{\partial x_k}u_i'\right)\left(\frac{\partial}{\partial x_k}u_j'\right)} && \text{dissipation.}
\end{aligned} \tag{12}$$

a. Higher-order terms

In Eq. (12), three new unknown higher-order turbulent correlations occur:

$$D_{ij} = -\frac{\partial}{\partial x_k}\overline{\rho}\overline{u_k'u_i'u_j'},$$

$$\pi_{ij} = \overline{u_j'\frac{\partial}{\partial x_i}P'} - \overline{u_i'\frac{\partial}{\partial x_j}P'},$$

$$\varepsilon_{ij} = 2\mu\overline{\left(\frac{\partial}{\partial x_k}u_i'\right)\left(\frac{\partial}{\partial x_k}u_j'\right)},$$

where D_{ij} describes the transport of the turbulent velocity correlations $\overline{u_i'u_j'}$ caused by the turbulent velocity fluctuations u_k'. In analogy to Eq. (2), a general expression for $\overline{u_k'u_i'u_j'}$ can be written as

$$\overline{u_k'u_i'u_j'} = -K_{ijklmn}\frac{\partial}{\partial x_n}\overline{u_{lm}'u'}.$$

The simplest possible expression for D_{ij}, which takes into account the assumed anisotropy between the vertical and the horizontal space direction is

$$D_{ij} = \frac{\partial}{\partial x_k}\overline{\rho}c_1K_k\frac{\partial}{\partial x_k}\overline{u_i'u_j'}, \quad \text{with} \tag{13}$$

$$K_1 = K_2 = c_0\lambda\sqrt{\frac{3}{2}E_{\text{hor}}},$$

$$K_3 = c_0\lambda\sqrt{3E_{\text{ver}}}. \tag{14}$$

Expression (13) is an extension of the expression used by Lewellen (1977). It preserves the tensor symmetry of D_{ij} but violates the symmetry in $\overline{u_k'u_i'u_j'}$. An additional empirical constant is denoted by c_1.

The effect of the pressure fluctuations on the turbulent velocity correlations is described by π_{ij}. Its physical

meaning can be better seen after a simple transformation:

$$\pi_{ij} = \frac{1}{\overline{\rho}}\left[\frac{\partial\overline{\rho}\overline{u_j' P'}}{\partial x_i} + \frac{\partial\overline{\rho}\overline{u_i' P'}}{\partial x_j} - \overline{P'\left(\frac{\partial\overline{\rho}u_j'}{\partial x_i} + \frac{\partial\overline{\rho}u_i'}{\partial x_j}\right)}\right]. \quad (15)$$

The integral of the first two terms over a volume surrounded by a laminar flow gives zero. Therefore, these terms result in a redistribution between turbulent velocity correlations and can be treated like diffusion terms (Mellor and Herring 1973). Following Hanjalic and Launder (1972), turbulent pressure correlations can be ignored except close to the wall.

The last two term in (15) do not contribute to the total turbulent energy because of the incompressibility assumption in (10). They only result in a redistribution between the components of the turbulent energy. The most common formulation is based on Rotta (1951) and acts in the direction of an isotropic turbulent energy distribution:

$$\pi_{ij} = c_2\overline{\rho}\frac{\sqrt{E}}{\lambda}\left(\overline{u_i' u_j'} - \delta_{ij}\frac{1}{3}E\right). \quad (16)$$

The effect of viscous dissipation on the turbulent velocity correlations, that is, the transition from turbulent motion to molecular motion, is described by ε_{ij}. Based on the idea of an inertial subrange turbulent energy is only dissipated by viscous forces and only transferred from larger to smaller scales in space. Therefore, the dissipation term ε_{ij} depends only on the energy transfer and not on the viscosity of the fluid. In the isotropic limit the dissipation of turbulent energy is determined by the total turbulent energy and a turbulent time scale τ_0, which only depends on the turbulent energy and the turbulent length scale (Mellor and Herring 1973). We extend this formulation by assuming that ε_{ij} is proportional to the components of the turbulent energy $\overline{u_i' u_i'}$ ($k = 1, 2, 3$). In addition we assume that the turbulent timescale $\tau_0 = \lambda/\sqrt{E}$ is an isotropic quantity of the flow:

$$\varepsilon_{ij} = c_3\overline{\rho}\frac{\sqrt{E}}{\lambda}\overline{u_i' u_j'}\delta_{ij}. \quad (17)$$

Similar formulations can be found in Daly and Harlow (1970) and Donaldson (1972). An empirical constant is denoted by c_3.

b. Production terms

Wind shear and buoyancy are responsible for the production of turbulent energy:

$$P_i = -2\overline{\rho}\overline{u_i' u_k'}\frac{\partial}{\partial x_k}\overline{u_i}, \quad (18)$$

$$P_\rho = -2g\overline{u_3'\rho'}. \quad (19)$$

The most common formulation for the turbulent velocity correlations under the assumption of local isotropy is (Mellor and Yamada 1974)

$$\overline{u_i' u_k'} = -K\left(\frac{\partial}{\partial x_k}\overline{u_i} + \frac{\partial}{\partial x_i}\overline{u_k}\right) + \frac{1}{3}E\delta_{ik}. \quad (20)$$

We treat the second-order correlation in P_i in analogy to the third-order correlation in D_{ij}. The simplest formulation for P_i that takes into account an anisotropy between horizontal and vertical space directions is

$$P_i = 2\overline{\rho}K_k\left(\frac{\partial}{\partial x_k}\overline{u_i}\right)\left(\frac{\partial}{\partial x_k}\overline{u_i}\right). \quad (21)$$

Stratification only contributes to the vertical component of turbulent energy. Thereby positive buoyancy produces and negative buoyancy deletes turbulent energy. In pure atmospheric applications the stratification is described by the gradient of the potential temperature. In our model we take into account the presence of active tracers by using the potential density σ. The potential density is the density of the mixture at a reference pressure. The potential density is not a conservative quantity under phase transitions that include the gas phase. However, those phase transitions change the vertical stratification of the fluid and therefore do not need to be reflected in the production of turbulent kinetic energy separately. For P_ρ, we yield

$$P_\rho = 2g\overline{\rho}K_\sigma\frac{1}{\overline{\sigma}}\frac{\partial}{\partial z}\overline{\sigma}, \quad \text{with} \quad (22)$$

$$K_\sigma = \alpha_\sigma K_3 = \alpha_\sigma c_0\lambda\sqrt{3E_{\text{ver}}},$$

$$\alpha_\sigma = \alpha_\theta q_g + \sum_{i=1}^{N_t}\alpha_i q_i, \quad (23)$$

where α_σ, α_θ, α_j denote the inverse Prandtl number for the mixture, for heat, and for each active tracer, respectively; q_g and q_i denote the mass mixing ratios for gas and each additional tracer, respectively.

c. Prognostic equations for turbulent kinetic energy

If we use Eq. (12) together with the higher-order terms in (13), (16), (17) and the production terms in (21), (22), and neglect molecular diffusion, we yield the following for the horizontal and vertical components of the turbulent kinetic energy (8) and (9):

$$\frac{\partial}{\partial t}E_{\text{hor}} = -\overline{u_k}\frac{\partial}{\partial x_k}E_{\text{hor}} \quad \text{advection}$$

$$+ \frac{1}{\overline{\rho}}\frac{\partial}{\partial x_k}\overline{\rho}c_1K_k\frac{\partial}{\partial x_k}E_{\text{hor}} \quad \text{turbulent diffusion}$$

$$+ 2K_k\left[\left(\frac{\partial}{\partial x_k}\overline{u_1}\right)^2 + \left(\frac{\partial}{\partial x_k}\overline{u_2}\right)^2\right] \quad \text{shear production}$$

$$
\begin{aligned}
&- c_2\frac{\sqrt{E}}{\lambda}\left(E_{\text{hor}} - \frac{2}{3}E\right) && \text{redistribution}\\
&- c_3\frac{\sqrt{E}}{\lambda}E_{\text{hor}} && \text{dissipation,} \quad (24)
\end{aligned}
$$

$$
\begin{aligned}
\frac{\partial}{\partial t}E_{\text{ver}} &= -\overline{u_k}\frac{\partial}{\partial x_k}E_{\text{ver}} && \text{advection}\\
&+ \frac{1}{\overline{\rho}}\frac{\partial}{\partial x_k}\overline{\rho}c_1K_k\frac{\partial}{\partial x_k}E_{\text{ver}} && \text{turbulent diffusion}\\
&+ 2K_k\left(\frac{\partial}{\partial x_k}\overline{u_3}\right)^2 && \text{shear production}\\
&- 2g\alpha_\sigma K_3\frac{1}{\overline{\sigma}}\frac{\partial}{\partial z}\overline{\sigma} && \text{production through buoyancy}\\
&- c_2\frac{\sqrt{E}}{\lambda}\left(E_{\text{ver}} - \frac{1}{3}E\right) && \text{redistribution}\\
&- c_3\frac{\sqrt{E}}{\lambda}E_{\text{ver}} && \text{dissipation.} \quad (25)
\end{aligned}
$$

The turbulent exchange coefficients K_k and K_σ are given by (6) and (23).

d. Turbulent length scale

The turbulent length scale is a characteristic length scale of turbulent eddies in an air parcel. Therefore, the turbulent length scale λ is considered a conservative quantity in the absence of sinks and sources (Daly and Harlow 1970). Commonly, the turbulence length scale is diagnosed locally [e.g., Agee and Gluhovsky (1999) and references therein]. In a volcanic plume, however, the time scales for advection are in the same order or shorter than those for turbulence. Hence, we include history-dependent effects of transport in the equation for the turbulent length scale. Since production and sink terms for the turbulent length scale are quite uncertain (Lewellen 1977), we choose a formulation where the production is driven by the deviation from an equilibrium length scale:

$$
\begin{aligned}
\frac{\partial}{\partial t}\lambda &= -\overline{u_k}\frac{\partial}{\partial x_k}\lambda && \text{advection}\\
&+ \frac{1}{\overline{\rho}}\frac{\partial}{\partial x_k}\overline{\rho}c_1K_k\frac{\partial}{\partial x_k}\lambda && \text{turbulent diffusion}\\
&- c_2\frac{\sqrt{E}}{\lambda}(\lambda - \lambda_0) && \text{equilibrium term,} \quad (26)
\end{aligned}
$$

with

$$
\begin{aligned}
\lambda_0 &= \min(0.67z,\ \Delta s,\ \lambda_0^*),\\
\lambda_0^* &= 0.54\sqrt{\frac{E}{N^2}},\\
N^2 &= -\frac{g}{\overline{\sigma}}\frac{\partial\overline{\sigma}}{\partial z},\\
\Delta s &= (\Delta x + \Delta y + \Delta z)/3.
\end{aligned}
$$

The equilibrium turbulent length scale λ_0 is limited by the distance to the ground z and the mean grid resolution Δs. For stable condition, that is, a positive Brunt–Väisälä frequency N^2, the equilibrium turbulent length scale is given according to Deardorff (1980).

e. Empirical constants and compressibility effects

The empirical constants can be determined from a variety of measurements. An often used set of constants is (Zilitinkevich et al. 1967; Mellor and Yamada 1974; Yu 1976; Lewellen 1977)

$$c_0 = 0.32, \qquad c_1 = 0.80, \qquad c_2 = 0.43, \quad (27)$$

Dickey and Mellor (1980) found in their measurements a reduction of the effective dissipation of turbulent energy with increasing stability. To take into account this effect we use the ratio of the turbulent length scale to the mean grid resolution, which is a dimensionless quantity that characterizes the influence of stability onto turbulence (Deardorff 1980):

$$c_3 = 0.067 + 0.18\frac{\lambda}{\Delta s}. \quad (28)$$

So far we have neglected turbulent pressure correlations $\overline{u_i'P'}$ and treated turbulent density correlations $\overline{u_i'\rho'}$ only in the buoyancy term. However, this is no longer true if the transport velocities are on the order of the speed of sound or greater. In the case of volcanic eruptions close to the vent, Mach numbers greater than 2 can be reached because the speed of sound is strongly reduced by the presence of high particle concentrations.

Intrinsic compressibility (nonzero divergence) of a turbulent velocity field tends to inhibit mixing and reduce the amplification rate of turbulent kinetic energy produced by a mean velocity gradient (Simone et al. 1997). According to Zeman (1990), observed Mach number effects can be treated as a correction to the empirical constant c_3 in the dissipation term

$$c_3^\star = c_3[1 + c_4F(M_t)], \quad (29)$$

with

$$
\begin{aligned}
F(M_t) &= \begin{cases} 1 - \exp\left[-\left(\dfrac{M_t - 0.1}{0.6}\right)^2\right] & \text{for } M_t > 0.1,\\ 0 & \text{else,}\end{cases}\\
M_t &= \frac{\sqrt{E}}{c_3}, \qquad c_4 = 0.75,
\end{aligned}
$$

where M_t is the turbulent Mach number and c_s the speed of sound.

The inverse Prandtl number α_x of a quantity x is the ratio between the turbulent exchange coefficients for this quantity and for momentum. For heat, α_θ is stability dependent. We follow Deardorff (1980):

$$\alpha_\theta = 1 + 2\frac{\lambda}{\Delta s}. \tag{30}$$

For each particulate tracer the inverse Prandtl number depends on particle properties such as size, shape, and surface roughness. Since particles possess a larger inertia than the surrounding gas molecules it is reasonable to assume that the turbulent exchange coefficients for particles are smaller than those for momentum. In our simulations we used for simplicity an inverse Prandtl number of $\alpha_i = 0.67$ for all particulate tracers.

4. Results

Previously we used ATHAM to simulate volcanic eruption plumes in a two-dimensional model version considering two ash particle classes of different sizes. In recent papers we analyzed the influence of environmental conditions on the volcanic plume rise (Graf et al. 1999) and studied the scavenging of volcanic particles (Textor 1999).

Here we show results from a three-dimensional simulation and discuss the simulated turbulent properties of the plume. In order to cover a larger range of particle sizes than in previous studies we increased the number of ash particle classes to three. Their sizes vary between 0.02 and 8 mm in diameter. The plume dynamic is influenced by the particle mass, which alters the mixture's buoyancy and the terminal velocities. At sea level atmospheric pressures the terminal fall velocities are 0.024, 3.2, and 15.2 m s^{-1} for small, medium, and large particles, respectively. The pressure decrease with altitude leads to an increase of the terminal velocities with altitude. At the tropopause level, the terminal velocities are increased to 0.62, 8.32, and 39.5 m s^{-1} for small, medium, and large particles, respectively (Herzog et al. 1998).

We chose a horizontal model domain of 250 and 200 km in x and y directions, respectively. The model top is located at 50-km altitude. The number of grid points is 127 in x and z directions and 107 in y direction. In order to achieve a spatial resolution of 100 m close to the volcano's vent, we use a stretched grid. Starting with 100-m vertical resolution at the vent, the spatial resolution increases to 300 and 550 m in 10- and 20-km altitude, respectively. In the horizontal, the spatial resolution increases from 100 m at the volcano to about 8 km in 100-km distance from the volcano. Since the x direction defines the mean wind direction, the volcano is shifted in x direction upwind from the model's center.

We initialize the model with vertical profiles for temperature, relative humidity, and horizontal wind under the assumption of a hydrostatic equilibrium. The initial conditions are horizontally homogeneous and represent a tropical atmosphere with the tropopause at 17-km altitude. A 45-min spinup ensures the adjustment of the flow around the volcano.

TABLE 1. Volcanic forcing.

Parameter	Value
Model domain (x, y, z)	250 km × 200 km × 50 km
Diameter of plume base	300 m
Velocity at plume base	250 m s^{-1}
Temperature at plume base	1073 K
Gas fraction	6% (by weight)
Water vapor fraction of total gas	50% (by weight)
Particle radius	
Small	0.01 mm
Medium	0.20 mm
Large	4.00 mm
Terminal fall velocity at 1000 mb	
Small	0.024 m s^{-1}
Medium	3.2 m s^{-1}
Large	15.2 m s^{-1}
Particle fraction	
Small	32% (by weight)
Medium	31% (by weight)
Large	31% (by weight)
Bulk density of erupting mixture after pressure adjustment	3.143 kg m^{-3}
Mass eruption rate	5.55 10^7 kg s^{-1}
Duration of eruption	1 h

The volcanic forcing is specified by a vertical velocity and the composition of the erupting mixture at the plume's base after pressure adjustment. The plume base is set to 300 m in diameter. The erupting mixture has a bulk density of 3.14 kg m^{-3}. Together with an exit velocity of 250 m s^{-1}, this results in a mass eruption rate of 5.55×10^7 kg s^{-1}. The complete volcanic forcing is listed in Table 1.

Our simulated eruption lasts for 1 h, which is considerably shorter than most real volcanic eruptions. However, at the end of the simulated eruption the plume starts to reach the model boundaries so that the open lateral boundaries begin to affect the simulation. For a longer simulation, the horizontal model domain and the number of horizontal grid points need to be enlarged, which would significantly increase the computing time. A more feasible approach would be to couple ATHAM with a regional model: boundary condition for ATHAM could be prescribed from the regional model; ash-removal processes in the distal diluted plume could be studied in the regional model.

In addition to the three-dimensional reference experiment, we perform sensitivity experiments in cylindrical coordinates.

a. The reference experiment in three dimensions

Before we discuss the turbulent quantities of the three-dimensional reference experiment we will briefly

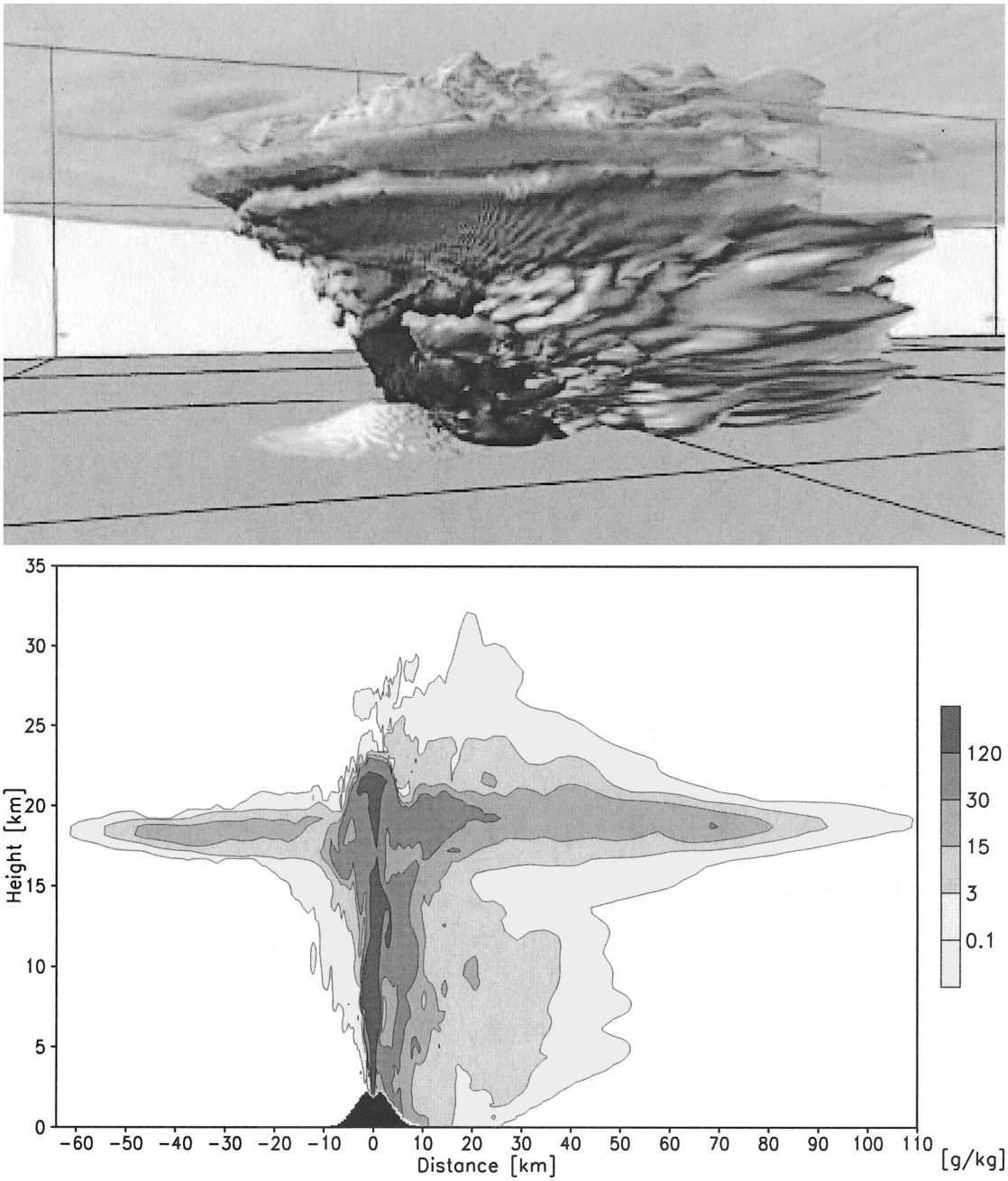

FIG. 1. Ash plume of particles of all sizes after 50 min of eruption. (upper) A three-dimensional image of the plume. (lower) Particle concentrations as a cross section through the same plume.

describe the ash plume after 50 min of eruption, which is shown in Fig. 1. Figure 1 (upper panel) shows a three-dimensional image of the plume. The observer's viewpoint is at 10-km altitude. The mean background wind blows from the left to the right side following the grid lines depicted on the ground. The umbrella region, which is seen from below consists mainly of fine ash particles. Larger particles (depicted in darker colors) leave the umbrella region rather quickly due to sedimentation or do not even reach the umbrella region. After 50 min of eruption only a negligible amount of the smallest ash particles (20 μm in diameter) has been deposited on the ground and only 1% of the medium-sized ash particles (400 μm in diameter). However, for the largest ash particles (8 mm in diameter) more than 60% of the erupted particles are already deposited on the ground.

Figure 1 (lower panel) shows the mass mixing ratio of ash particles in the x–z plane located at the volcano's center. Again, the mean horizontal wind in the back-

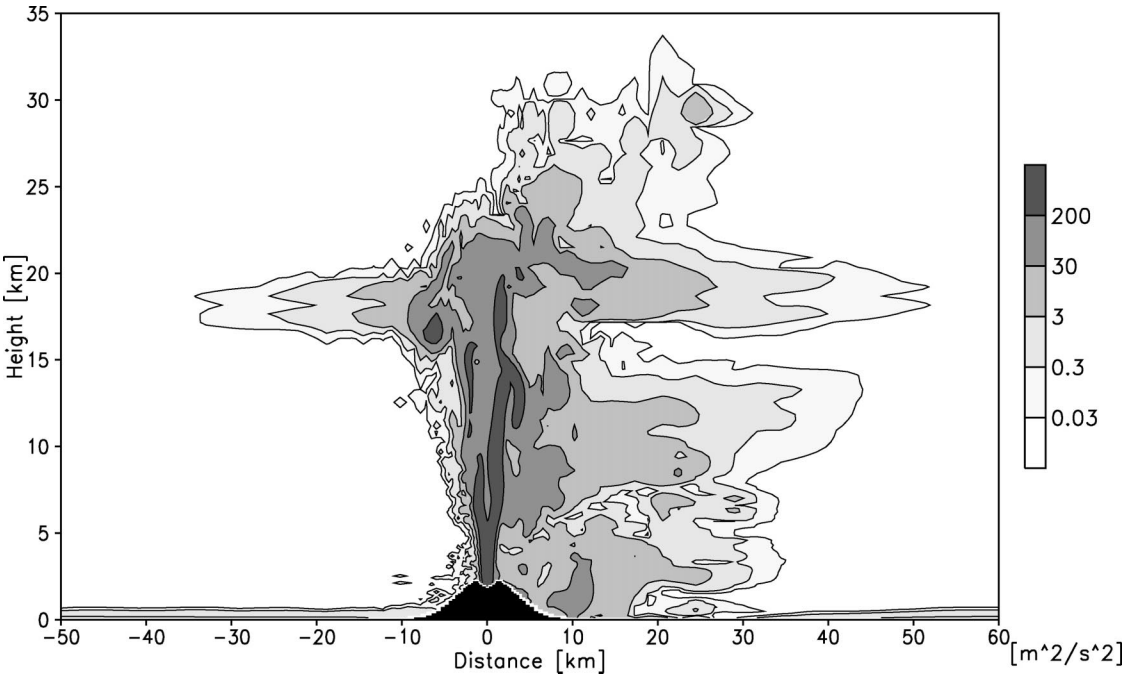

FIG. 2. Vertical turbulent energy after 50 min of eruption.

ground blows from the left to the right with maximum wind speeds of 25 m s^{-1} in the jet region below the tropopause. The ash plume reaches an altitude of over 32 km. The umbrella region, which marks the neutral buoyancy height, spreads out between 18- and 19-km altitude, reaching slightly lower altitudes on the upwind side of the volcano. The plume has an asymmetric form. The leading edge traveled 110 and 65 km from the volcano to the downwind and upwind side, respectively.

Figures 2 to 4 show the prognostic turbulent quantities after 50 min of eruption. The plots show the same *x*–*z* plane as in Fig. 1, but with a smaller horizontal

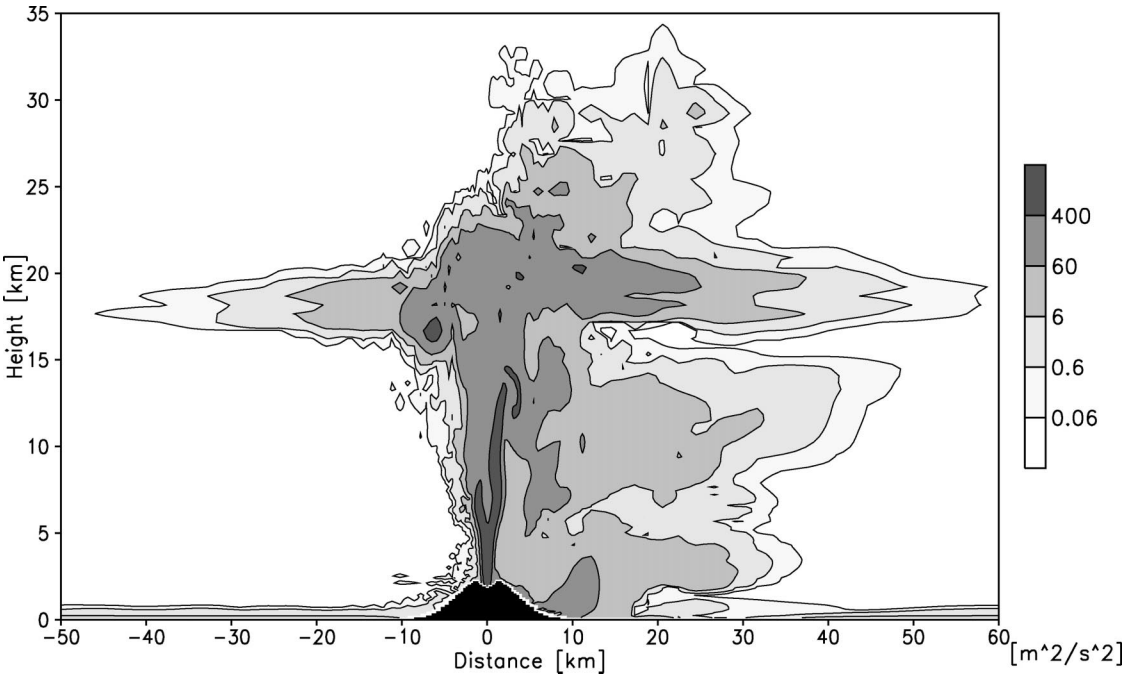

FIG. 3. Horizontal turbulent energy after 50 min of eruption.

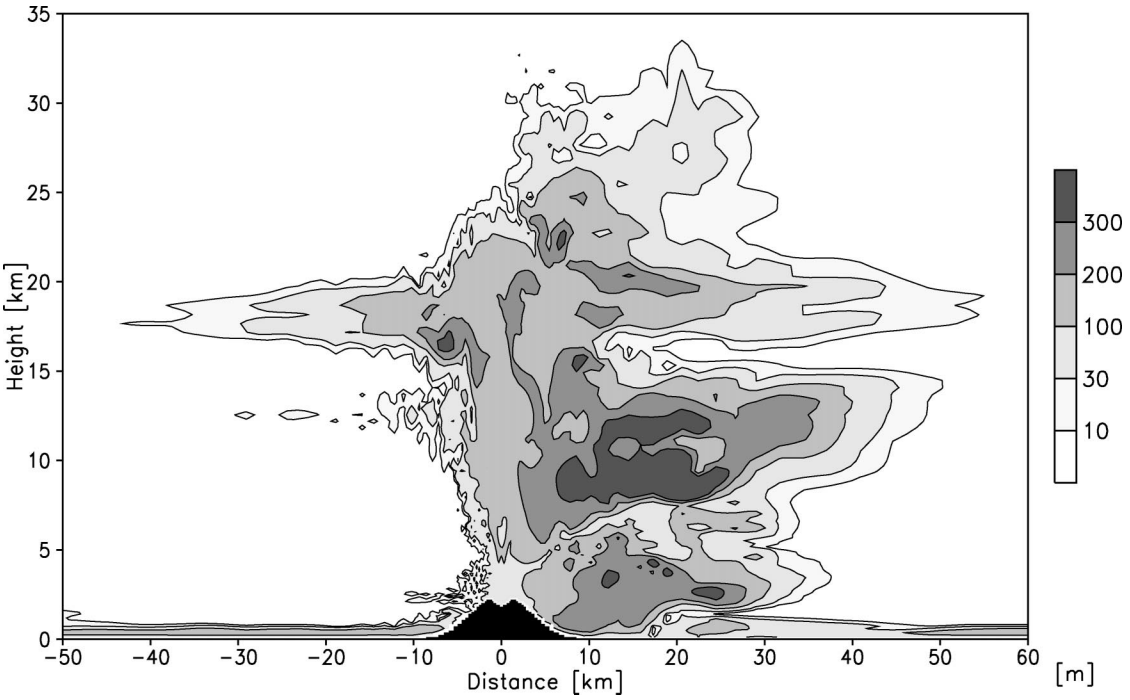

FIG. 4. Turbulent length scale after 50 min of eruption.

extent. The contour intervals for the vertical and horizontal turbulent energy (Fig. 2 and 3) differ by a factor of 2 so that, in the case of a local isotropy, both plots would look exactly the same.

Large values of turbulent quantities are well confined within the plume. In addition elevated values are noticeable in the lowest kilometer of the model atmosphere indicating the formation of a turbulent boundary layer.

Within the plume the turbulent energies vary by more than five orders of magnitude. Close to the vent, maximum values well above 2000 $m^2\ s^{-2}$ are reached within the ascending zone. By the time the erupted mixture reaches the stratosphere, the turbulent energies are reduced by almost two orders of magnitude. The turbulent length scale, on the other hand, shows in the ascending zone lower values close to the vent and increasing values with increasing altitude. Within the umbrella region the turbulent energies decrease with increasing distance from the plume base; on average the turbulent energies decrease one order of magnitude every 10–15 km.

Despite the general similarities between the horizontal and turbulent energy there are substantial deviations from a local isotropy. In case of a local isotropy, the total turbulent energy can be calculated in three ways: from the vertical turbulent energy, the horizontal turbulent energy, or from the sum of horizontal and vertical turbulent energies,

$$E_{\text{turb}} = \frac{3}{2}E_{\text{hor}} = 3E_{\text{ver}} = E_{\text{hor}} + E_{\text{ver}}.$$

The anisotropy in the turbulent energy can be expressed by

$$\gamma = 100\frac{\frac{3}{2}E_{\text{hor}} - 3E_{\text{ver}}}{E_{\text{hor}} + E_{\text{ver}}}.$$

This quantity is shown in Fig. 5. Within the ascending zone above the vent the vertical turbulent energy is considerably larger than in the isotropic limit with γ greater 100% in large areas. Here, vertical turbulent exchange processes are more important than horizontal turbulent exchange processes. For the most part of the umbrella region, the opposite is the case: horizontal turbulent exchange is more important than vertical turbulent exchange.

Figures 6 and 7 show the time scales connected with subscale turbulence. The turbulent time scales are related to the mean grid resolution Δs in the following way: $\tau = \Delta s^2/2K_{\text{turb}}$, where K_{turb} is either the vertical or horizontal turbulent exchange coefficient.

Although the contour intervals in Figs. 6 and 7 are on a quasi-logarithmic scale, the previously discussed anisotropy is also apparent from the turbulent time scales. In addition, Figs. 6 and 7 illustrate the relative importance of turbulent mixing in different plume regions; close to the vent adjacent grid points exchange information due to turbulence on time scales of seconds, within the ascending zone, on time scales shorter than a minute. Within the umbrella region and farther away from the ascending zone the time scales for turbulence

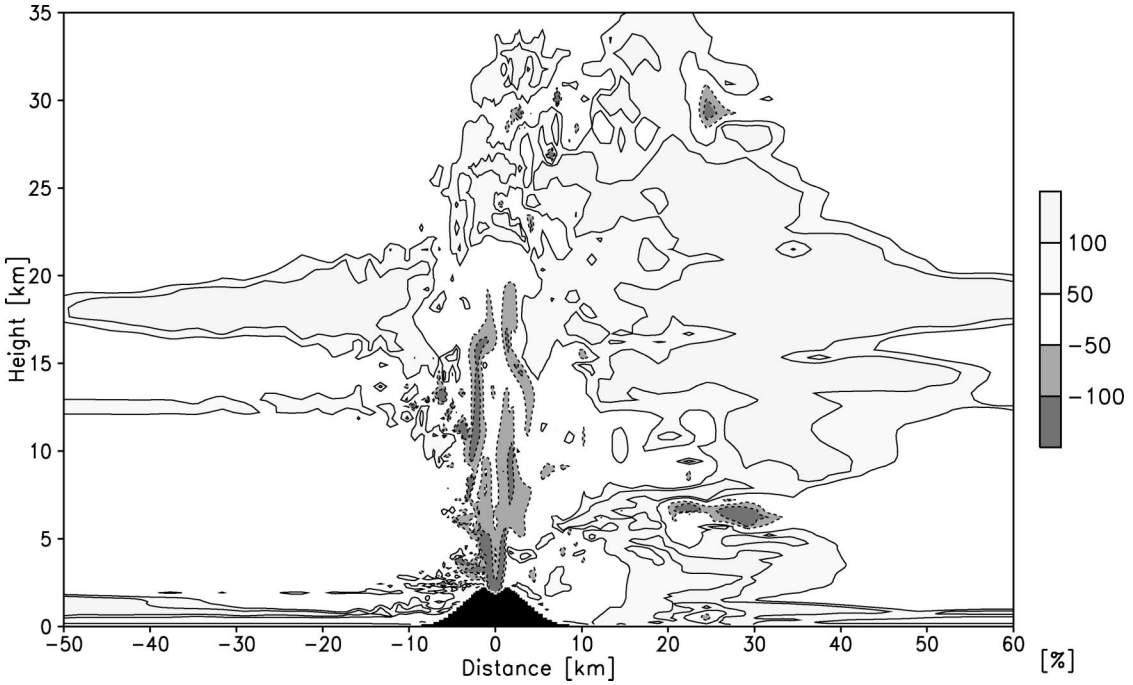

FIG. 5. Anisotropy in turbulent energy (%): $100\{[(3/2)E_{hor} - 3E_{ver}]/(E_{hor} + E_{ver})\}$.

rapidly increase to several hours. On the downwind side, the leading edge of the plume traveled 110 km away from the location of the volcano within 50 min of eruption. Already at 40 km away from the source, the time scale for turbulence exceeds 1 day. Because we perform simulations for 1 to 2 h, effects of turbulence influence the simulation only within or close to the ascending zone where ash particles stay for a couple of minutes due to the large flow velocities in that region.

The differences between horizontal and vertical turbulent energy have a significant impact on the entrainment rates. This impact is the greatest within the as-

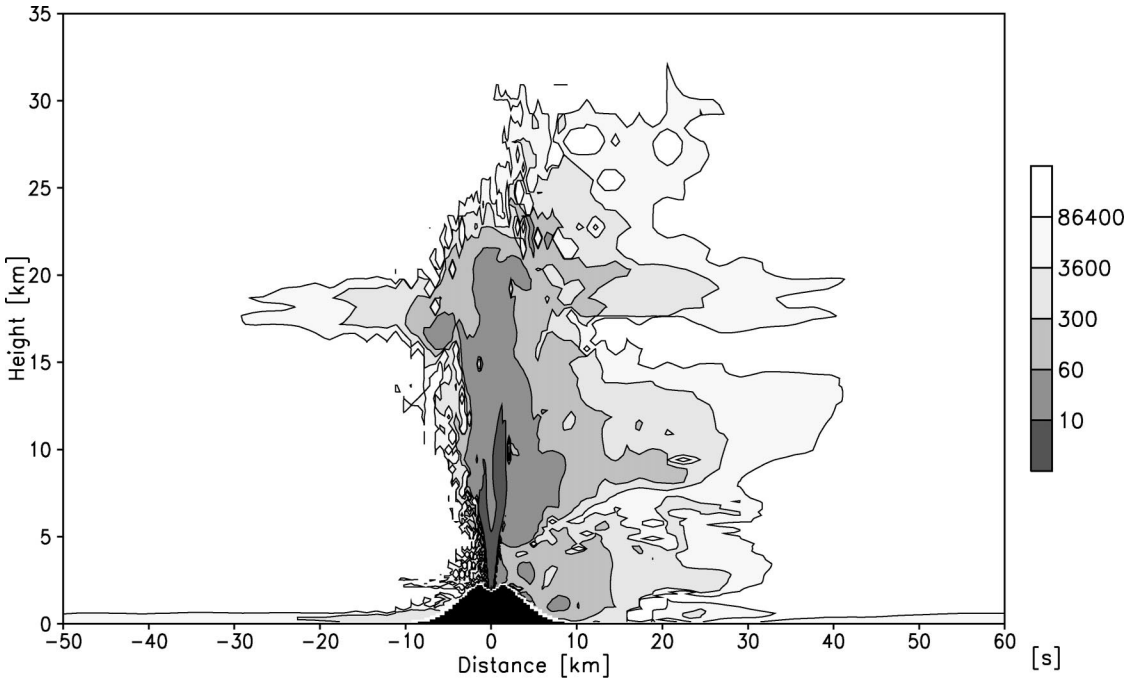

FIG. 6. Time scale for vertical turbulent exchange after 50 min of eruption.

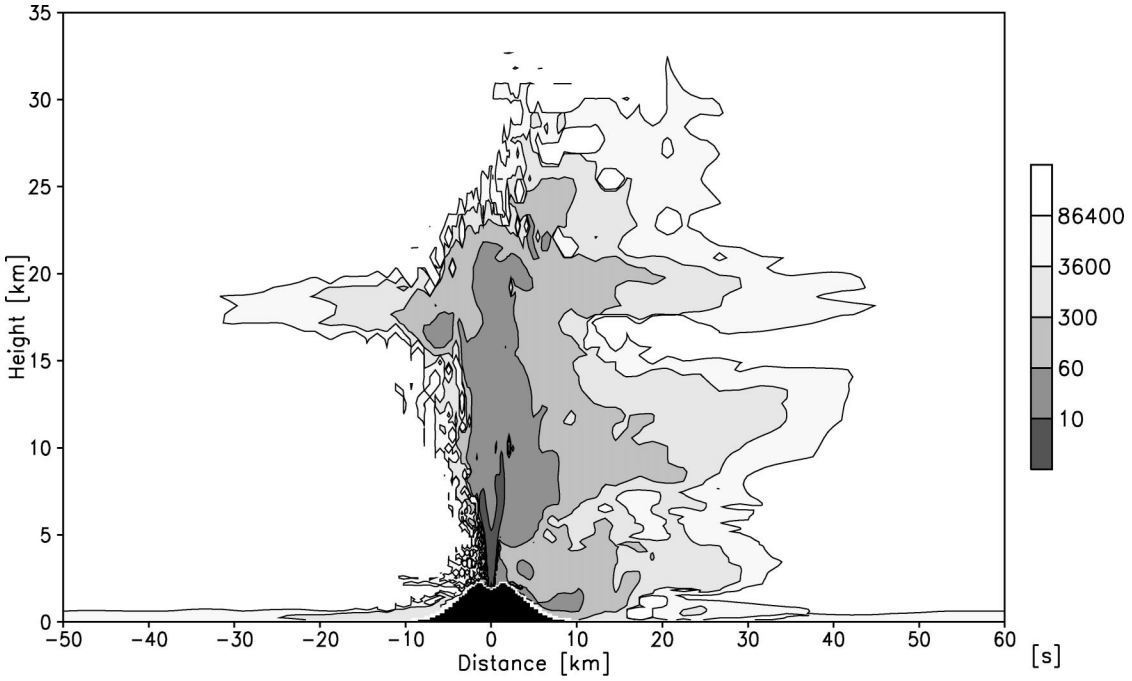

FIG. 7. Time scale for horizontal turbulent exchange after 50 min of eruption.

cending zone above the vent where turbulent mixing is most intense. Here, the anisotropy between vertical and horizontal turbulence leads to a weaker horizontal mixing than in the isotropic limit. A smaller horizontal entrainment not only delays the plume from becoming buoyant but also reduces the amount of ambient water vapor in the plume. The amount of water determines to a large extent microphysical processes within the plume: condensation of water vapor increases the buoyancy of the plume through the release of latent heat (Graf et al. 1999); the interaction of hydrometeors with volcanic gases and particles leads to efficient particle aggregation and scavenging of volcanic particles and gases (Textor et al. 2003). Except under very dry conditions most of the water vapor within the plume originates from the ambient atmosphere (Glaze et al. 1997; Herzog et al. 1998). Because most of the water vapor is located in the lower part of the atmosphere an accurate description of entrainment in the ascending zone is crucial for the description of microphysical processes within the plume.

b. The impact of nonlocal effects in turbulence in cylindrical coordinates

We performed a series of simulations in order to investigate the importance of a detailed subgrid-scale turbulence scheme, the sensitivity of empirical constants, and the impact of nonlocal effects in the turbulence scheme. Because of computer restrictions, these tests were done in cylindrical coordinates. In cylindrical coordinates a mean background wind cannot be considered. However, such a two-dimensional simulation corresponds to a three-dimensional simulation with an atmosphere initially at rest. Here we only discuss the impact of nonlocal effects on the plume development.

Figure 8 shows the mass mixing ratio of fine ash 50 min after the eruption started for the reference experiment in cylindrical coordinates (top) and the simulation with the isotropic turbulence scheme (bottom). The isotropic turbulence scheme is a simplification of our more complex scheme: only the total turbulent kinetic energy is predicted. The turbulent length scale is determined diagnostically applying the expression for λ_0 in Eq. (26). Supersonic effects, as well as the effects of active tracers on turbulence, are not taken into account.

Although the anisotropic and the isotropic turbulence schemes produce almost an identical neutral buoyancy height in the umbrella region, there are substantial differences between the two simulations. With the isotropic scheme, the plume height (measured by the maximum height of the 5 g kg^{-1} isoline) is 4.5 km or 20% lower than in the reference experiment. The leading edge of the plume travels faster in the isotropic simulation, and the plume covers an area 14% larger than in the anisotropic simulation.

However, more interesting than the differences in plume shape and more important for microphysical processes within the plume are the structural differences within the ascending zones of both simulations. In the reference experiment the ascending zone is unsteady and more structured than in the isotropic experiment. At 15-km altitude there is an instability that leads to a partial plume collapse. The ash particles leaving the ascending

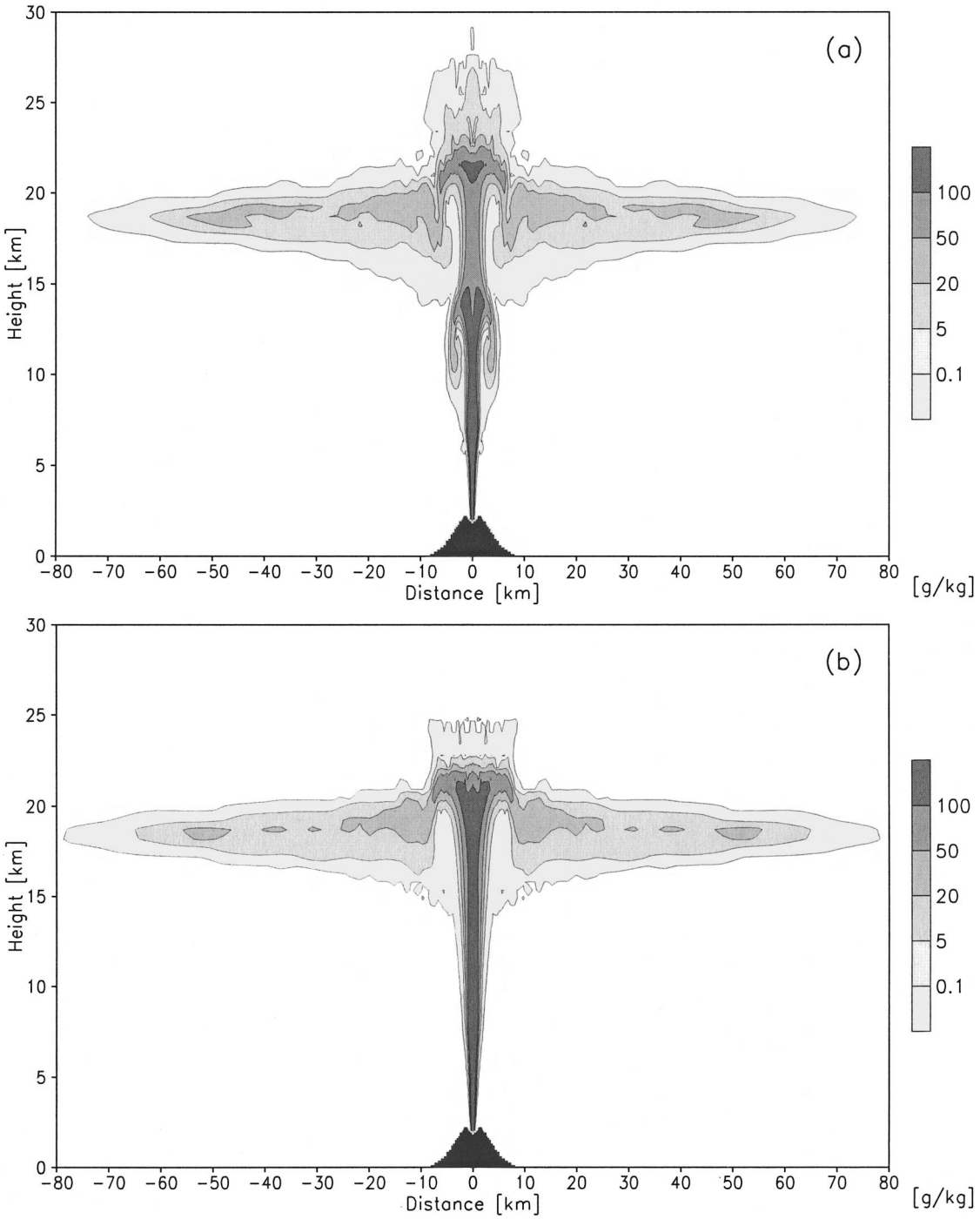

FIG. 8. Fine ash concentration after 50 min of eruption. (a) The ash plume in the axisymmetric reference experiment; (b) the ash plume for the experiment with the simplified, isotropic turbulence scheme.

zone are re-entrained into the ascending zone between 5- and 12-km altitude. This instability, however, is not located at a constant altitude but moves upward with time, disappears and is reformed again between 7- to 8-km altitude. The resulting pumping motion also allows the ash particles to reach higher altitudes than in the experiment with isotropic turbulence scheme.

When the isotropic turbulence scheme is applied the horizontal entrainment is stronger in the lower part of the ascending zone so that no instability is formed. In addition, more water vapor is entrained into the plume at lower altitudes. Although the plume's total water burden is only 7% larger than in the reference experiment, substantially larger concentrations of hydrometeors are

obtained within the upper part of the ascending zone where they play a key role in the scavenging of volcanic gases and particles (Textor et al. 2003).

5. Summary and conclusions

The new turbulence scheme presented here distinguishes between horizontal and vertical turbulent exchange processes. It is based on a set of three coupled prognostic equations for the horizontal and vertical turbulent kinetic energy and the turbulent length scale. In the isotropic limit this scheme corresponds to the traditional turbulent kinetic energy (TKE) approaches with one prognostic turbulent kinetic energy.

The numerical simulations of a typical Plinian volcanic eruption plume in three dimensions with ATHAM reveal that turbulent processes are well confined within the plume. The turbulent kinetic energy varies over several orders of magnitude. The time scales for turbulence are in the order of seconds close to the vent, and increase to several hours and days within the umbrella region. The substantial differences between horizontal and vertical turbulent exchange suggest that the local anisotropy of turbulence has an important impact on the plume development.

A simplified version of the presented turbulence scheme, which resembles the traditional isotropic TKE approaches, does not reproduce the instabilities in the ascending zone and the fine structure of the plume as seen in the reference experiment with the full turbulence scheme. These instabilities and the fine structure are particularly important if processes within the plume are considered such as scavenging of volcanic particles and gases.

Unfortunately, no observational dataset for volcanic plumes exists that would allow for an independent proof that our new more complex turbulence scheme produces a more realistic simulation than a traditional TKE scheme. However, our new scheme is more general than a traditional TKE scheme. The new scheme treats the main history-dependent nonlocal effects of turbulence. In atmospheric turbulence, vertical stratification is very important and makes turbulent processes acting in the vertical distinctively different from those acting in horizontal space directions. The complete treatment of these nonlocal effects is the main advantage of the computationally very expensive, fully second-order turbulence schemes in atmospheric and technological problems (Lewellen 1977; Speziale 1987). In addition, our new scheme has been successfully used in a simulation of an observed biomass burning plume (Trentmann et al. 2002).

Since the presented turbulence scheme is not specially tailored for the description of volcanic eruption plumes or plumes in general, this scheme is also suitable for a wide range of atmospheric applications. In particular, when the anisotropy in turbulence cannot be ignored, our turbulence scheme allows us to differentiate between horizontal and vertical turbulent exchange processes without requiring a fully second-order turbulence scheme.

Acknowledgments. This study was initially sponsored by the Volkswagen–Stiftung Grant EVA (Emission of Volatiles to the Atmosphere). In addition, we thank the University of Michigan for providing computing time and Prof. Joyce Penner for the opportunity to complete this study.

REFERENCES

Agee, E., and A. Gluhovsky, 1999: LES model sensitivities to domains, grids, and large-eddy timescales. *J. Atmos. Sci.,* **56,** 599–604.

Bretherton, C. S., and Coauthors, 1999: An intercomparison of radiatively driven entrainnment and turbulence in a smoke cloud, as simulated by different numerical models. *Quart. J. Roy. Meteor. Soc.,* **125,** 391–423.

Daly, B. J., and F. H. Harlow, 1970: Transport equations in turbulence. *Phys. Fluids,* **13,** 2634–2649.

Deardorff, J. W., 1980: Stratocumulus-capped mixed layers derived from a three-dimensional model. *Bound.-Layer Meteor.,* **18,** 495–527.

Dickey, T. D., and G. L. Mellor, 1980: Decaying turbulence in neutral and stratified fluids. *J. Fluid Mech.,* **99,** 13–31.

Donaldson, C. duP., 1972: Calculation of turbulent shear flows for atmospheric and vortex motions. *AIAA J.,* **10,** 4–12.

Glaze, L. S., S. M. Baloga, and L. Wilson, 1997: Transport of atmospheric water vapor by volcanic eruption columns. *J. Geophys. Res.,* **102,** 6099–6108.

Graf, H.-F., M. Herzog, J. M. Oberhuber, and C. Textor, 1999: The effect of environmental conditions on volcanic plume rise. *J. Geophys. Res.,* **104,** 24 309–24 320.

Hanjalic, K., and B. E. Launder, 1972: Fully developed asymmetric flow in a plane channel. *J. Fluid Mech.,* **51,** 301–335.

Harsha, P. T., 1977: Kinetic energy methods. *Handbook of Turbulence,* W. Frost and T. H. Molden, Eds., Plenum Press, 187–236.

Herzog, M., H.-F. Graf, C. Textor, and J. M. Oberhuber, 1998: The effect of phase changes of water on the development of volcanic plumes. *J. Volcanol. Geotherm. Res.,* **87,** 55–74.

Kolmogorov, A. M., 1942: The equations of turbulent motion in an incompressible fluid. *Izv. Acad. Sci. USSR,* **6,** 56–58.

Lewellen, W. S., 1977: Use of invariant modeling. *Handbook of Turbulence,* W. Frost and T. H. Molden, Eds., Plenum Press, 237–290.

Mellor, G. L., and H. J. Herring, 1973: A survey of the mean turbulent field closure models. *AIAA J.,* **11,** 590–599.

——, and T. Yamada, 1974: A hierarchy of turbulence closure models for planetary boundary layers. *J. Atmos. Sci.,* **31,** 1791–1806.

Moeng, C. H., and Coauthors, 1996: Simulation of a stratocumulus-topped planetary boundary layer: Intercomparison among different numerical codes. *Bull. Amer. Meteor. Soc.,* **77,** 261–278.

Monin, A. S., and A. M. Yaglom, 1971: *Statistical Fluid Mechanics—Mechanics of Turbulence.* Vol. 1, MIT Press, 769 pp.

Oberhuber, J. M., M. Herzog, H.-F. Graf, and K. Schwanke, 1998: Volcanic plume simulation on large scales. *J. Volcanol. Geotherm. Res.,* **87,** 29–53.

Prandtl, L., and K. Wieghardt, 1945: Über ein neues Formelsystem für die ausgebildete Turbulence. *Nach. Akad. Wiss. Göttingen Math. Phys.,* **K1,** 6–19.

Rotta, J. C., 1951: Statistische Theorie nichthomogener Turbulenz. *Z. Phys.,* **129,** 547–572.

Simone, A., G. N. Coleman, and C. Cambon, 1997: The effect of compressibility on turbulent shear flow: A rapid-distortion-theory and direct-numerical-simulation study. *J. Fluid Mech.,* **330,** 307–338.

Speziale, C. G., 1987: On nonlinear *k–l* and *k–ϵ* models of turbulence. *J. Fluid Mech.,* **178,** 459–475.

——, 1998: Turbulence modeling for time-dependent RANS and VLES: A review. *AIAA J.,* **36,** 173–184.

Textor, C., 1999: Numerical simulation of scavenging processes in explosive eruption clouds. Ph.D. thesis, University of Hamburg, 129 pp.

——, H.-F. Graf, M. Herzog, and J. M. Oberhuber, 2003: Injection of gases into the stratosphere by explosive volcanic eruptions. *J. Geophys. Res.,* in press.

Trentmann, J., M. O. Andreae, H.-F. Graf, P. V. Hobbs, and R. D. Ottmar, 2002: Simulation of a biomass-burning plume: Comparison of model results with observations. *J. Geophys. Res.,* **107,** 4013, doi:10.1029/2001JD000410.

Yu, T. W., 1976: Numerical studies of the atmospheric boundary layer with a turbulent energy closure scheme. Preprints, *Third Symp. on Atmospheric Turbulence, Diffusion and Air Quality,* Rayleigh, NC, Amer. Meteor. Soc., 53–59.

Zeman, O., 1990: Dilatation dissipation: The concept and application in modeling compressible mixing layers. *Phys. Fluids,* **2,** 178–188.

Zilitinkevich, S. S., D. L. Laikhtman, and A. S. Monin, 1967: Dynamics of the atmospheric boundary layer. *Izv. Atmos. Oceanic Phys.,* **3,** 170–191.